UCLA
UCLA Previously Published Works

Title
Characterization of spatial distortion in a 0.35 T MRI-guided radiotherapy system

Permalink
https://escholarship.org/uc/item/3df3q8hd

Journal
Physics in Medicine and Biology, 62(11)

ISSN
0031-9155

Authors
Ginn, John S
Agazaryan, Nzhde
Cao, Minsong
et al.

Publication Date
2017-06-07

DOI
10.1088/1361-6560/aa6e1a

Peer reviewed

eScholarship.org Powered by the California Digital Library
University of California

Author Manuscript

Author Manuscript

Author Manuscript

Author Manuscript

HHS Public Access

Author manuscript

Phys Med Biol. Author manuscript; available in PMC 2018 July 26.

Published in final edited form as:

Phys Med Biol. 2017 June 07; 62(11): 4525–4540. doi:10.1088/1361-6560/aa6e1a.

Characterization of spatial distortion in a 0.35 T MRI-guided radiotherapy system

John S Ginn[1,4], **Nzhde Agazaryan**[1], **Minsong Cao**[1], **Umar Baharom**[2], **Daniel A Low**[1], **Yingli Yang**[1], **Yu Gao**[3], **Peng Hu**[3], **Percy Lee**[1], and **James M Lamb**[1]

[1]Department of Radiation Oncology, David Geffen School of Medicine, University of California, Los Angeles, CA 90095, United States of America

[2]Integrated Medical Technologies, Troy, NY 12180, United States of America

[3]Department of Radiological Sciences, David Geffen School of Medicine, University of California, Los Angeles, CA 90095, United States of America

Abstract

Spatial distortion results in image deformation that can degrade accurate targeting and dose calculations in MRI-guided adaptive radiotherapy. The authors present a comprehensive assessment of a 0.35 T MRI-guided radiotherapy system's spatial distortion using two commercially-available phantoms with regularly spaced markers.

Images of the spatial integrity phantoms were acquired using five clinical protocols on the MRI-guided radiotherapy machine with the radiotherapy gantry positioned at various angles. Software was developed to identify and localize all phantom markers using a template matching approach. Rotational and translational corrections were implemented to account for imperfect phantom alignment. Measurements were made to assess uncertainties arising from susceptibility artifacts, image noise, and phantom construction accuracy.

For a clinical 3D imaging protocol with a 1.5 mm reconstructed slice thickness, 100% of spheres within a 50 mm radius of isocenter had a 3D deviation of 1 mm or less. Of the spheres within 100 mm of isocenter, 99.9% had a 3D deviation less than 1 mm. 94.8% and 100% of the spheres within 175 mm were found to be within 1 mm and 2 mm of the expected positions in 3D respectively. Maximum 3D distortions within 50 mm, 100 mm and 175 mm of isocenter were 0.76 mm, 1.15 mm and 1.88 mm respectively. Distortions present in images acquired using the real-time imaging sequence were less than 1 mm for 98.1% and 95.0% of the cylinders within 50 mm and 100 mm of isocenter. The corresponding maximum distortion in these regions was 1.10 mm and 1.67 mm.

These results may be used to inform appropriate planning target volume (PTV) margins for 0.35 T MRI-guided radiotherapy. Observed levels of spatial distortion should be explicitly considered when using PTV margins of 3 mm or less or in the case of targets displaced from isocenter by more than 50 mm.

[4] Author to whom any correspondence should be addressed., jginn@mednet.ucla.edu.

Supplementary material for this article is available online (Some figures may appear in colour only in the online journal)

Author Manuscript Author Manuscript Author Manuscript Author Manuscript

Keywords

MRI; radiotherapy; quality assurance

1. Introduction

On-line magnetic resonance imaging (MRI) guidance for radiation therapy provides a number of potential benefits including excellent soft tissue contrast for precise alignment, target tracking for respiratory and cardiac motion compensation, (Cervino et al 2011, Stam et al 2012, Seregni et al 2016) monitoring of tumor progression or regression and normal tissue response with on-board functional imaging, (Kupelian and Sonke 2014, Nguyen et al 2014, Yang et al 2016) and treatment plan adaptation (Dowling et al 2012). However, inhomogeneities in the magnetic field due to imperfect shimming, eddy currents and non-linear gradients will adversely affect the scanner's spatial integrity resulting in reduced targeting accuracy and potentially reducing dose calculation accuracy (Spees et al 2011, Walker et al 2015). Additionally, patient-specific image distortion may also arise from spin populations characterized by different chemical shifts and magnetic susceptibility effects (Dietrich et al 2008, Stanescu et al 2012). Unfortunately, phantom studies cannot perfectly replicate the magnetic susceptibility and chemical shift effects present in patient anatomy, but they can assess compromised spatial distortion due to field inhomogeneity, eddy currents and non-linear gradients. This work presents the net distortion resulting from these effects, but does not measure their contributions independently.

The authors present a comprehensive phantom-based spatial distortion assessment of images produced by the MRIdian MRI-guided radiotherapy system (ViewRay, Inc., Oakwood Village, OH). Three dimensional (3D) spatial distortion was assessed using a commercially-available phantom containing a 3D matrix of spheres produced by Integrated Medical Technologies (Troy, NY). Volumetric image sets of the phantom were acquired using the two most commonly used clinical protocols on the system. The locations of the spheres were obtained using custom software and compared to the ground-truth locations of the spheres based on the phantom specifications and computed tomography (CT) scans. The difference between the position found by the software and the ground truth location provides a metric to assess the spatial distortion of the scanner. In a similar manner, the distortions present in a single plane (2D) real-time imaging protocol were evaluated using a commercially-available 2D spatial integrity phantom containing a single grid of contrast-filled cylinders manufactured according to AAPM recommendations (Price et al 1990). Our results expand upon work previously published by others which evaluated the scanner's spatial distortion at 26 discrete locations on the surface of a 200 mm and 350 mm diameter sphere (Hu et al 2015). Our evaluation informs considerations of the accuracy of patient alignment, tumor tracking, and dose calculations used for MRI-guided adaptive radiotherapy. The 3D distortion analysis results were compared to results from the 2D spatial integrity phantom and analysis software provided by ViewRay Inc. for periodic machine quality assurance. Tolerances and regions of interest analyzed in this work should be viewed in the context of typical treatments at our institution as well as professional society recommendations. The report of the American Association of Physicists in Medicine Task Group on Linear

Author Manuscript Author Manuscript Author Manuscript Author Manuscript

Accelerator Quality Assurance (TG-142) recommends image distortion and imaging-to-radiation isocenter coincidence of 1 mm for image-guided stereotactic body radiotherapy (SBRT) and stereotactic radiotherapy (SRS) treatments, and 2 mm for non-SRS/SBRT treatments. This evaluation should be viewed in the context of typical target sizes, locations with respect to isocenter, and planning target volume (PTV) margins used in MRI-guided radiotherapy. For example, in 10 consecutive patients recently treated on the MRIdian at our institution, median tumor longest axis length was 50 mm (range: 24–140 mm) and median distance from center of the tumor to machine isocenter was 21 mm (range: 2–49 mm). The median PTV margin used was 4 mm (range: 3–10 mm). 7 of the 10 patients were treated with SBRT, and 7 with image-based gating.

2. Methods

Distortion measurements are obtained by acquiring images of the 3D and 2D distortion phantoms (section 2.3), localizing the markers in the phantoms using custom software (sections 2.4 and 2.5), and evaluating the difference between the measured location and the ground truth location of each marker (section 2.6). Additionally, we estimate measurement uncertainty due to noise and finite voxel size, phantom-specific susceptibility artifacts, and phantom construction (sections 2.7–2.9). Sections 2.1 and 2.2 describe the MRIdian device and the phantoms used, respectively.

2.1. MRIdian system

The MRIdian system combines a 0.35 T split bore scanner with a radiation therapy gantry using three cobalt-60 sources (Mutic and Dempsey 2014). The magnet was designed by ViewRay and produced by Agilent Technologies (Santa Clara, CA) for the first 3 devices including the one studied in this manuscript, and subsequently by Japan Superconductor Technology, Inc. (Kobe, Japan). The gradient coil was designed by ViewRay and manufactured by Tesla Engineering (Storrington, United Kingdom). The scanner control software, reconstruction software, and radiofrequency coils and amplifiers were supplied by Siemens Medical Systems (Erlangen, Germany)[5].

The MRIdian provides 21 clinical imaging protocols for 3D images and 9 protocols for 2D real-time imaging. All clinical protocols utilize the manufacturer provided balanced steady state free precession sequence (bSSFP), with various combinations of field of view (FOV), slice thickness, and other acquisition parameters that yield different signal to noise ratios (SNR), with the exception of a single gradient echo sequence protocol with a very small FOV which is not used clinically at our institution. Real-time imaging is performed in a single sagittal plane at 4 frames s^{-1}. Sagittal planes with lateral separation up to ±270 mm from isocenter can be imaged.

2.2. Spatial integrity phantoms

The commercially available 3D spatial integrity phantom has been described in detail elsewhere (Huang et al 2016) and its construction is summarized here. The phantom

[5]Private communication with ViewRay Engineer.

Author Manuscript Author Manuscript Author Manuscript Author Manuscript

contains a grid of hollow spheres embedded in an acrylic substrate. The phantom was constructed from 9 stacked acrylic plates each with 513 spheres arranged in a single plane. The 8 mm diameter hollow spheres are connected in a matrix with hollow tubes, and are located 16 mm apart. Viewed in axial cross-section, there are 21 horizontal rows of spheres with varying numbers of spheres in each row as shown in figure 1.

The nominal width precision of the acrylic plates was 0.1 mm. The spheres and connecting rods were carved out of the acrylic plates using a CNC machine, with a nominal precision of 0.025 mm in each of the three dimensions (Huang et al 2016). The matrix was filled with 0.4 mM NiCl aqueous solution that results in a field inhomogeneity of 0.85 ppm due to its molar magnetic susceptibility of 6145×10^{-6} cm^3 mol^{-1} (Huang et al 2016). The presence of air bubbles in the phantom was noted by Huang et al, potentially reducing the accuracy of sphere localization. In order to minimize bubbles, the matrix was filled by joining and sealing the plates in an acrylic superstructure while entirely submerged in NiCl solution. Additionally, the manufacturer increased the diameter of the spheres from 7 mm (as in Huang et al (2016)) to the present value of 8 mm. The sphere located in the center row, slice and column was aligned to isocenter. This sphere served as the reference location to calculate the ground truth sphere positions. Using this alignment of the phantom, the most distal spheres from isocenter along each anatomical axis were ±64 mm in the inferior–superior direction, ±160 mm in the anterior–posterior direction and ±208 mm laterally.

The 2D spatial integrity phantom was manufactured by Fluke Biomedical (Everett, WA). This phantom contains a single plane of cylinders carved out of a sheet of acrylic and submerged in an approximately 18.02 mM $CuSO_4$ aqueous contrast agent characterized by a magn etic susceptibility of 1460×10^{-6} cm^3 mol^{-1} (Lide 2003). The phantom contains a 288 mm by 288 mm grid of 397 cylinders spaced approximately 14.5 mm apart with a diameter of approximately 13 mm and depth of about 25 mm. The 397 cylinders form a 20 × 20 cylinder grid, with one cylinder ‘missing’ in the 8th, 9th and 13th rows of the phantom. The phantom was manufactured to meet AAPM specifications for periodic MRI quality assurance (Price et al 1990).

2.3. Data acquisition

The 3D spatial integrity phantom was imaged with the two 3D image protocols which are most commonly used at our institution. Imaging was repeated at five gantry angles: 0, 30, 60, 90 and 120°. The gantry angle was varied because the magnetically susceptible materials in the gantry are not uniformly distributed and may affect the field homogeneity and thus spatial integrity of the scanner. Table 1 reports relevant acquisition parameters and the simulated readout gradient amplitude for each scanning protocol.

Both protocols implement phase and slice partial Fourier techniques, and the 3 mm reconstruction slice thickness scan implements GRAPPA parallel imaging (Griswold et al 2002) to shorten the acquisition duration of the scans. The 3 mm reconstructed slice thickness image requires 25 s to acquire and is most commonly used clinically for breath hold imaging of anatomic locations subject to respiratory motion. The 1.5 mm reconstructed slice thickness image is acquired for 172 s and is used for anatomic locations not subject to

Author Manuscript Author Manuscript Author Manuscript Author Manuscript

respiratory motion. The gradient corrections provided by Siemens were applied for both protocols to minimize image distortions during image reconstruction.

Real-time imaging sequences were evaluated using the 2D spatial integrity phantom aligned with the sagittal cardinal axis. Relevant acquisition parameters for the three real time imaging protocols used in this study are summarized in table 2.

All 2D imaging protocols also use GRAPPA parallel imaging and phase partial Fourier techniques to accelerate the image acquisition. Off-median sagittal planes that do not intersect isocenter may be used during treatments to track off-isocenter targets, therefore scans were conducted shifting the phantom in 9 mm intervals to ± 99 mm laterally. For each acquisition, 100 preparation images were conducted to ensure the magnetization reached steady state conditions prior to acquiring 40 test images. These 40 images were averaged to form a single image during the analysis process in order to reduce noise.

2.4. Phantom marker localization—3D images

The spheres were localized in the phantom images using a template matching approach. A spherical template model was stepped within the images to find the locations of local maximum normalized correlation coefficients (Briechle and Hanebeck 2001). The 3.0 mm reconstructed slice thickness images were linearly interpolated to construct a 3D dataset with 1.5 mm reconstructed slice thicknesses. Each phantom marker was only considered localized if the correlation coefficient exceeded a pre-determined threshold. Thresholding prevented image noise from being identified as a sphere. Thresholding also had the effect of omitting spheres located in an image artifact such as banding or blurring (see arrows in figure 2).

Correlation coefficient thresholds of 0.75 and 0.70 were used for the 1.5 mm and 3.0 mm reconstructed slice thickness images, respectively. These values struck the best balance between omitting spheres in regions of artifacts while retaining the spheres not in these locations. Any spheres in these regions remaining in the analysis were then manually removed. To improve computational efficiency, an individual search sub-volume was defined for each sphere, searching 6 mm in each direction from the calculated ground-truth sphere location. It was visually verified that all the spheres in the phantom were within the bounds of the search regions. After template matching localized spheres to the nearest 1.5 × 1.5 × 1.5 mm voxel, images were up-sampled by a factor of 3 using cubic interpolation in a region of interest (ROI) about the sphere, and template matching was repeated in that ROI to refine the sphere position. Finally, the sphere position was further refined to be the center of mass position of each sphere’s up-sampled voxels weighted by the MRI signal. This calculation used all adjacent voxels within a 12 mm sided cubic ROI about the position found using template matching. For spheres located near the wall of the phantom a 8 mm sided cubic ROI was used to calculate their final position to avoid signal in the adjacent wall. This smaller cubic ROI was also used for the 7 centermost spheres in the phantom to avoid a phantom imperfection that resulted in a consistent signal artifact located between the spheres.

Author Manuscript Author Manuscript Author Manuscript Author Manuscript

In order to correct for imperfect phantom alignment, a rotational and translational correction was performed using Procrustes method (Goodall 1991). Field homogeneity is expected to decease further from isocenter and at locations away from the central cardinal planes. Only spheres lying on the centermost axial, sagittal and coronal planes were used to align the phantom with the ground truth positions. The transformation extracted from Procrustes method using these spheres was applied to all sphere positions.

2.5. Phantom marker localization—real time images

The real time images were analyzed using a similar process to the methods described above for 3D images. Because of the low native resolution of the real-time imaging protocol, images were up-sampled by a factor of seven to improve cylinder localization accuracy through template matching. Cylinder locations were not refined using a center of mass approach because the space between adjacent cylinders was smaller than the image pixel spacing. A correlation threshold was applied to avoid including cylinders found in regions of severe blurring or signal loss when the phantom was shifted far from isocenter (see arrow in figure 3).

This correlation threshold was empirically selected to be 0.65 and any remaining cylinders severely affected by these signal abnormalities were manually removed. To correct for any misalignment or rotation of the phantom, Procrustes method was implemented to minimize any global offset between the found and known locations.

2.6. Spatial distortion analysis

To evaluate image deformation, the sphere locations determined by the software were compared to the ground-truth location of the spheres. Ground truth locations were calculated according to the phantom specifications and updated by computed tomography (CT) scans of the phantoms as described below. Distortion was analyzed in regions of interest (ROI) of 50 mm, 100 mm, and 175 mm about the isocenter, as well as in the entire 3D phantom.

The longitudinal slab thickness of the 3D phantom was 128 mm; thus only the ROI of 50 mm radius constituted a sphere. Within each ROI, distortion was quantified by the mean value, maximum value, and percent passing a specified threshold of 1 or 2 mm. For the 3D images, both 3D distortion and 2D distortion in the axial plane were quantified. For the real-time images, 2D distortion in the sagittal plane was quantified.

2.7. Measurement uncertainty estimate

At least 3 factors may affect the accuracy of our results: sphere localization uncertainty due to finite voxel size and/or image noise, inaccuracy in phantom construction, and susceptibility artifacts in the phantom images. Susceptibility artifacts are true image distortions, but susceptibility distortions in the phantom are treated as measurement uncertainty because the susceptibility distortions in the phantom are not likely representative of patient-specific susceptibility distortions.

The combination of localization uncertainty and construction uncertainty was estimated by measuring the distances between the sphere aligned to isocenter and the surrounding six

Author Manuscript Author Manuscript Author Manuscript Author Manuscript

spheres. The root-mean-square deviation of distances was multiplied by $\frac{\sqrt{3}}{\sqrt{2}}$ to account for the fact that each distance measurement combines 3 spatial dimensions and localization of 2 spheres. Only the central 7 spheres were used because highest field homogeneity and lowest image distortion are expected at the image isocenter.

The effect of image noise was quantified by comparing sphere locations in a repeated scan.

2.8. Measurement uncertainty estimate—susceptibility artifacts

To determine the magnitude of susceptibility effects, two scans were acquired of the 3D phantom with reversed gradient polarity. When the gradients are reversed, distortion artifacts resulting from magnetic susceptibility will occur in the reversed direction (Sakurai et al 1992). The difference between locations of the spheres found in these two scans provides an estimate of the severity of magnetic susceptibility effects for our phantom.

2.9. Measurement uncertainty estimate—phantom CT scans

To evaluate the accuracy of phantom construction, CT images of both phantoms were acquired using a Siemens SOMATOM Definition AS 64. Because of the large size of the 3D spatial integrity phantom, the images were acquired with the phantom rotated 90° (aligned along the sagittal plane) to reduce the attenuation of the beam and thereby prevent photon-starvation artifacts and reduce noise. The 2D planar phantom is smaller in length and cross section and was aligned with the axial plane for imaging. The 3D phantom was imaged at a 0.78 × 0.78 mm resolution, 1 mm slice thickness, with a 140 kVp and 575 effective mAs, the largest effective mAs allowed by the scanner for an object of that length. The 2D phantom was imaged with a 0.98 × 0.98 mm resolution, 3 mm slice thickness, 140 kVp and 1400 effective mAs. The locations of the spheres in the 3D phantom, and cylinders in the 2D phantom were determined using the analysis software. Because of the reduced contrast between the plastic and aqueous solution in the CT images, the weighted sum localization method was not implemented. The spheres in the 3D spatial integrity phantom were located via template matching, upscaling the images by a factor of three. Similarly, the cylinders in the 2D phantom were localized using the template matching approach, up-sampling the image by a factor of seven. Correlation thresholding was not implemented to remove spheres from the analysis of the CT images. However, some spheres contained air pockets that shifted the found location of the sphere away from its position in the image. These spheres were manually removed and omitted from the analysis. The same rotation and translation correction method applied during the MR analyses were implemented for these scans, and the same analysis metrics were computed for the CT analyses. The deviation between the found locations and expected locations refects both uncertainties localizing the spheres and cylinders in the CT images, as well as the imperfections of phantom construction. The CT of each phantom was also used to update the assumed spacing between the spheres and cylinders to construct the ground truth locations of the markers in subsequent analyses. Motivated by an observed linear trend in the CT-measured deviations, a systematic offset to the nominal inter-marker distance was determined using an iterative minimization of the global average CT-measured deviation.

Author Manuscript Author Manuscript Author Manuscript Author Manuscript

3. Results

3.1. Spatial distortion analysis—3D images

Table 3 provides summary metrics of spatial distortion measurements. Sphere localization uncertainty corresponding to these measurements was estimated to be 0.07 mm in the 1.5 mm reconstructed slice thickness images, and 0.28 mm in the 3 mm reconstructed slice thickness images according to deviation from expected distance between the seven centermost spheres. Localization error due to noise, phantom-specific susceptibility effects and phantom construction imperfections were approximately 0.07 mm, 0.11 mm and 0.28 mm respectively for the 1.5 mm reconstructed slice thickness scan (see sections 3.3–3.5 for more detail).

All the spheres inside the 175 mm radius region of interest were localized, passing the correlation threshold for each scanning protocol. The deviation between the scans acquired at different gantry angles was small (median: <0.1 mm), and the values reported above are the average values across these scans. Further detail is provided in the supplementary data (stacks.iop.org/PMB/62/4525/mmedia). Figures 4 and 5(a) shows the measured 2D and 3D distortion, respectively, in the entire phantom as a function of 2D and 3D radius from the central axis and isocenter, respectively, for the 1.5 mm reconstructed slice thickness image with the gantry positioned at 0°. Figure 5(b) shows the 3D image distortion in the centermost axial plane with the gantry positioned at 0° using the 1.5 mm slice thickness scan. This deformation field map was calculated by linearly interpolating the measured distortion at locations lying between the sphere markers.

The average 2D deviations within 50 mm, 100 mm and 175 mm of the central axis across all gantry angles were 0.34 mm, 0.36 mm and 0.46 mm using the 1.5 mm scan, and found to be 0.40 mm, 0.41 mm and 0.51 mm respectively for the 3.0 mm scan. As expected from considerations of magnetic field homogeneity, spatial distortion worsens with increasing distance from the isocenter. Of the entire phantom, 98.1% of spheres were localized in the 1.5 mm reconstructed slice thickness image and 98.1% of spheres were localized in the 3 mm reconstructed slice thickness image. Sphere localization failures occurred where the spheres were obscured by image artifacts at the edge of the image field of view (indicated in figure 2).

3.2. Spatial distortion analysis—real time images

Distortion measurements of the 2D phantom in the real time images using the 5 mm slice thickness protocol are summarized in table 4. The interested reader is encouraged to reference the supplementary data section for the same results using the 7 mm and 10 mm slice thickness protocols. Distortion in all 2D images with lateral shifts up to ±99 mm was analyzed as a single dataset in terms of ROIs defined by 3D distance to isocenter. The deviation of the cylinders from their expected positions acquired across all lateral shifts is shown as a function of distance from isocenter in figure 6(a). The average deviation for all cylinders was found to be 0.83 mm. An example 40-image average of the 2D phantom along with the cylinder found and ground truth locations is shown in figure 3. The corresponding

Author Manuscript Author Manuscript Author Manuscript Author Manuscript

2D deformation field map for this scan is shown in figure 6(b) and was calculated by linearly interpolating the measured distortion at positions falling in between the cylindrical markers

3.3. Measurement uncertainty estimate

The root-mean-square measured distances between the central sphere and six adjacent spheres yielded a combined construction accuracy and localization accuracy of 0.07 mm and 0.28 mm for the 1.5 mm and 3.0 mm reconstructed slice thickness images, respectively. The average 3D deviation between a pair of scans repeated using the 1.5 mm reconstructed slice thickness protocol, indicating the uncertainty contribution due to image noise, was 0.07 mm over the entire phantom volume.

3.4. Measurement uncertainty estimate—susceptibility artifacts

Uncertainties due to phantom-specific susceptibility-related distortion were taken to be half the average distance between locations of each marker in two scans acquired with opposite readout gradient polarities. The resulting uncertainties were 0.05 mm, 0.06 mm 0.08 mm and 0.11 mm within ROI of 50 mm, 100 mm, 175 mm of isocenter and the entire volume, respectively.

3.5. Measurement uncertainty estimate—phantom CT scans

Analysis of the CT images of the 3D spatial integrity phantom revealed that the deviation between the measured and nominal locations increased as a function of distance from iso-center. Although this is a feature that might be expected in MR images due to decreased field homogeneity further from isocenter, this result was not expected in CT images. This trend was removed by iteratively changing the assumed distance between the spheres along each dimension until the average deviation reached a minimum. Although phantom specifications state that the spacing between the spheres should be 16.00 mm, this technique indicated an actual spacing of 16.01 mm in the medial-lateral direction, 16.05 mm in the anterior–posterior direction and 16.08 mm in the inferior–superior direction. These values were used for all MRI analyses. These systematic offsets are consistent with expected precision of the CNC milling process used for phantom construction (Huang et al 2016) as well as thermal expansion resulting from differences in ambient temperature between phantom construction and imaging. Using these values the average 3D deviations in the CT scan of the phantom were found to be 0.20 mm, 0.22 mm, 0.24 mm within a 50 mm, 100 mm and 175 mm radius of isocenter respectively. The average deviation for all spheres was 0.28 mm.

When the CT analysis was performed for the 2D spatial integrity phantom, the deviation also increased as a function of distance from isocenter. This trend was removed using a spacing between the cylinders of 14.57 mm instead of 14.50 mm stated in the specifications. This value was used for both the CT analysis and all subsequent MR analyses of the 2D phantom. The analysis of the 2D spatial integrity phantom CT revealed the average deviation of the cylinders within 50 mm, 100 mm and 175 mm of isocenter and entire volume was 0.08 mm, 0.07 mm, 0.09 mm and 0.09 mm respectively.

Author Manuscript Author Manuscript Author Manuscript Author Manuscript

4. Discussion

Spatial distortion results in two distinct types of errors for MRI-guided radiation therapy. First, spatial distortion in the vicinity of the target results in targeting inaccuracy, both in initial positioning and in gating if applicable. Second, if the MRI is used for dose calculation then spatial distortion can result in dosimetric error. If electron density is inferred by bulk density assignment or using a deformably registered CT scan, distortions in the MRI images will yield an inaccurate mapping of the patient electron density. Our results indicate that 3D spatial distortion is sub-millimetric within 50 mm of isocenter, and slightly exceeds 1 mm for only less than 1% of spheres within 100 mm of isocenter when using the 1.5 mm reconstructed slice thickness scan. Measured distortion increased when using the 3.0 mm reconstructed slice thickness scan. Distortions present in images acquired using the real-time imaging sequence were less than 1 mm for 98.1% and 95.0% of the cylinders within 50 mm and 100 mm of isocenter. The uncertainty in sphere localization during the 3D analysis was estimated to be 0.07 mm and 0.28 mm for the 1.5 mm and 3.0 mm reconstruction slice scans respectively. Localization error due to noise, phantom-specific susceptibility effects and phantom construction imperfections were approximately 0.07 mm, 0.11 mm and 0.28 mm respectively for the 1.5 mm reconstructed slice thickness scan.

Spatial distortion arises from gradient non-linearity, main-field inhomogeneity, and eddy currents. Eddy currents and non-linear gradients potentially give rise to sequence-specific dist ortion, therefore a set of sequences representative of all the 3D and real-time 2D sequences available on the MRIdian for clinical use were analyzed. Spatial distortion in the clinical setting cannot be perfectly replicated with phantom measurements due to variations in shimming and the difference between the magnetic susceptibility and chemical shift effects present in the phantom compared to patient anatomy. Any residual inhomogeneity in the magnetic field following shimming will result in image distortions, but these effects are typically less severe than distortions caused by other effects such as gradient non-linearity (Wang et al 2004). Additionally, B_0 inhomogeneities scale with field strength, thus the 0.35 T MRIdian is less susceptible to these effects compared to higher field strength scanners, where more advanced techniques such as real time shimming may be required (van Gelderen et al 2007, Wachowicz et al 2010). However, because of the split-bore magnet design of the MRIdian, with a 30 cm gap between magnets, field homogeneity is expected to be worse compared to a 0.35 T continuous cylindrical magnet. Susceptibility artifacts worsen with increasing field strength and are most pronounced at tissue air interfaces. Simulations have been conducted for a number of different regions within the body characterized by differing magnetic susceptibility properties. One study showed that the maximum distortion on a 0.5 T bore scanner with 5 mT/m gradients was 0.57 mm due to susceptibility effects (Stanescu et al 2012). This value does not directly describe the susceptibility effects that are encountered on the MRIdian because it is a 0.35 T split-bore scanner, but it may provide an estimate of the order of magnitude of the deformation encountered in the clinic in regions subject to severe susceptibility effects.

Eddy currents may cause distortion, artifacts and signal losses in balanced steady state free precession sequences, the severity of which is dependent upon the gradient amplitude and waveform that vary depending on the pulse sequence and acquisition parameters. The

Author Manuscript Author Manuscript Author Manuscript Author Manuscript

balanced steady state free precession sequence is known to be susceptible to image artifacts and signal losses that result from eddy currents when the *k*-space acquisition is not linear. However, it has been shown that these effects can be largely minimized by acquiring *k*-space in sequential order or by paring the acquisition of *k*-space lines (Bieri et al 2005). The bSSFP sequences implemented for clinical scanning by the MRIdian utilize a linear acquisition of *k*-space.

This work reports a more comprehensive assessment of the ViewRay MRIdian's spatial distortion compared to previously published reports. Hu et al reported a valuable overall characterization of the MRIdian's imaging performance, including some spatial distortion measurements. Their measurements were limited to 26 points the surface of 200 mm and 350 mm diameter spheres for high resolution volumetric images, and 8 points on the perimeter of similarly sized circles in 3 isocenter-intersecting orthogonal planes for real time cine images (Hu et al 2015). Our work evaluates image distortion throughout the volume of a 3D phantom with 4617 markers spaced 16 mm apart, and a 2D phantom with 397 markers spaced 14.5 mm apart shifted to numerous off-isocenter locations. Hu et al reported maximum distortions of 1 and 1.8 mm, respectively, on the smaller and larger spherical surfaces. Our maximum distortion measurements over the same volumes were slightly larger (1.15 and 1.88 mm), which could result from the increased number of spatial points sampled. Importantly, the work of Hu et al did not report measurements in the region where the target will most likely be placed (i.e. within 50 mm of isocenter). Additionally, Hu et al did not assess the effect of noise, phantom-specific susceptibility effects and phantom construction inaccuracies on image distortion measurements.

The results of our software were cross checked against the results of a ViewRay-provided software in the transverse plane intersecting the isocenter. The ViewRay software analyzes distortion in high-resolution images of the 2D spatial integrity phantom. It is important to note that the ViewRay analysis software is not intended for use with (and does not work on) either real-time cine images, or images of the 3D spatial integrity phantom. The ViewRay analysis software yielded mean 2D spatial distortion in the transverse plane passing through isocenter of 0.24 mm and 0.39 mm in circles of radius 100 mm and 175 mm, respectively. The corresponding values from our 3D phantom analysis were 0.23 mm and 0.39 mm, respectively, showing excellent agreement in the small region where the two analyses overlap.

Our results may be useful to other clinics wishing to establish appropriate margins for their clinical MRI guided radiotherapy protocols. The observed level of distortion is small with respect to the 5 mm planning target volume (PTV) margins typically used for MRI guided stereotactic body radiotherapy (SBRT) in our clinic. American Association of Physicists in Medicine Task Group 142 recommends that geometric distortion in cone-beam CT image guidance be less than 1 mm for SBRT and no more than 2 mm for non-stereotactic treatments (Klein et al 2009). Weygand et al recommended a limit of 1 mm of spatial distortion in the vicinity of the PTV and a looser tolerance further from the target (Weygand et al 2016). In our clinic, targets are generally kept within 50 mm of isocenter, although they may occasionally be greater than 50 mm from isocenter due to the patient positioning limitations imposed by the presence of the 700 mm diameter bore of the MRIdian. Rarely if

Author Manuscript Author Manuscript Author Manuscript Author Manuscript

ever are targets treated greater than 100 mm from isocenter. Thus the effects of spatial distortion on targeting are safe with respect to PTV margins currently used but should be explicitly considered if PTV margins are further reduced below 5 mm. For considerations of dose calculation accuracy, 2D distortion at the edges of the patient volume is important because it could lead to inaccurate assignment of air-containing voxels as tissue, or vice versa. 2D distortion ranges from 0.36 mm to 0.46 mm as distance from the central axis extends from 100 mm to 175 mm in the 1.5 mm reconstruction slice images, comprising a typical range of patient body habitus in the axial plane. Considering that a Co-60 beam is attenuated approximate 3% cm^{-1} in water, this 2D distortion corresponds to a dose error of 0.11–0.14%.

5. Conclusion

The spatial distortion of images from a commercially-available 0.35 T MRI-guided radiation was measured using commercial phantoms and custom software developed for this purpose[6]. Tables 3 and 4 should be referred to by the medical physicist in conjunction with the radiation oncologist to inform appropriate planning target volume (PTV) margins for MRI-guided radiotherapy with the MRIdian. Spatial distortion arising from field inhomogeneity, eddy currents and gradient non-linearity was sub-millimetric in the vicinity of the target using a 3D imaging protocol with a 1.5 mm reconstructed slice thickness, as long as the target is within 50 mm of isocenter. Distortion within 100 mm of isocenter was less than 1 mm for more than 99% of the phantom markers using the 3D imaging protocols. Maximum distortions in the 3D protocols were 0.89 mm, 1.22, and 1.98 mm within 50 mm, 100 mm, and 175 mm radius from isocenter, respectively. Distortions in 2D were no greater than 1.10 mm within 50 mm of isocenter using the real time imaging sequence used for gating during treatment. Observed levels of spatial distortion should be explicitly considered when using PTV margins of 3 mm or less or in the case of targets displaced from isocenter by more than 50 mm.

Acknowledgments

James M Lamb has received consulting fees from ViewRay, unrelated to this work. Percy Lee, Minsong Cao and Yingli Yang have received speaking fees from ViewRay. Peng Hu receives research funding from ViewRay.

References

Bieri O, Markl M and Scheffer K 2005 Analysis and compensation of eddy currents in balanced SSFP *Magn*. Reson. Med. 54 129–37

Briechle K and Hanebeck UD 2001 Template matching using fast normalized cross correlation Proc. SPIE Optical Pattern Recognition XII 4387 95–102

Cervino LI, Du J and Jiang SB 2011 MRI-guided tumor tracking in lung cancer radiotherapy Phys. Med. Biol 56 3773–8521628775

Dietrich O, Reiser MF and Schoenberg SO 2008 Artifacts in 3 T MRI: physical background and reduction strategies Eur. J. Radiol 65 29–3518162353

Dowling JA, Lambert J, Parker J, Salvado O, Fripp J, Capp A, Wratten C, Denham JW and Greer PB 2012 An atlas-based electron density mapping method for magnetic resonance imaging (MRI)-alone

[6]Publicly available at: https://github.com/johnginn

Author Manuscript Author Manuscript Author Manuscript Author Manuscript

treatment planning and adaptive MRI-based prostate radiation therapy Int. J. Radiat. Oncol. Biol. Phys 83 e5–1122330995

Goodall C 1991 Procrustes methods in the statistical-analysis of shape J. R. Stat. Soc. B 53 285–339

Griswold MA, Jakob PM, Heidemann RM, Nittka M, Jellus V, Wang J, Kiefer B and Haase A 2002 Generalized autocalibrating partially parallel acquisitions (GRAPPA) Magn. Reson. Med 47 1202–1012111967

Hu Y 2015 Characterization of the onboard imaging unit for the first clinical magnetic resonance image guided radiation therapy system Med. Phys 42 5828–3726429257

Huang KC, Cao Y, Baharom U and Balter JM 2016 Phantom-based characterization of distortion on a magnetic resonance imaging simulator for radiation oncology Phys. Med. Biol 61 774–9026732744

Klein EE 2009 Task Group 142 report: quality assurance of medical accelerators Med. Phys 36 4197–21219810494

Kupelian P and Sonke JJ 2014 Magnetic resonance-guided adaptive radiotherapy: a solution to the future Semin. Radiat. Oncol 24 227–3224931098

Lide DR 2003 CRC Handbook of Chemistry and Physics: A Ready-Reference Book of Chemical and Physical Data (Boca Raton, FL: CRC Press)

Mutic S and Dempsey JF 2014 The ViewRay system: magnetic resonance-guided and controlled radiotherapy Semin. Radiat. Oncol 24 196–924931092

Nguyen ML 2014 The potential role of magnetic resonance spectroscopy in image-guided radiotherapy Frontiers Oncol. 4 91

Price RR, Axel L, Morgan T, Newman R, Perman W, Schneiders N, Selikson M, Wood M and Thomas SR 1990 Quality assurance methods and phantoms for magnetic resonance imaging: report of AAPM nuclear magnetic resonance Task Group No. 1 Med. Phys 17 287–952333055

Sakurai K, Fujita N, Harada K, Kim SW, Nakanishi K and Kozuka T 1992 Magnetic susceptibility artifact in spin-echo MR imaging of the pituitary gland AJNR Am. J. Neuroradiol 13 1301–8 (PubMed: 1414819)1414819

Seregni M, Paganelli C, Lee D, Greer P B, Baroni G, Keall P J and Riboldi M 2016 Motion prediction in MRI-guided radiotherapy based on interleaved orthogonal cine-MRI *Phys.* Med. Biol 61 872–87

Spees WM, Buhl N, Sun P, Ackerman JJ, Neil JJ and Garbow J R 2011 Quantification and compensation of eddy-current-induced magnetic-field gradients J. Magn. Reson 212 116–2321764614

Stam MK, Crijns SP, Zonnenberg BA, Barendrecht MM, van Vulpen M, Lagendijk JJ and Raaymakers BW 2012 Navigators for motion detection during real-time MRI-guided radiotherapy Phys. Med. Biol 57 6797–80523032581

Stanescu T, Wachowicz K and Jaffray DA 2012 Characterization of tissue magnetic susceptibility-induced distortions for MRIgRT Med. Phys 39 7185–9323231269

van Gelderen P, de Zwart JA, Starewicz P, Hinks RS and Duyn JH 2007 Real-time shimming to compensate for respiration-inducedB0 fuctuations Magn. Reson. Med 57 362–817260378

Wachowicz K, Stanescu T, Thomas SD and Fallone BG 2010 Implications of tissue magnetic susceptibility-related distortion on the rotating magnet in an MR-linac design Med. Phys 37 1714–2120443492

Walker A, Liney G, Holloway L, Dowling J, Rivest-Henault D and Metcalfe P 2015 Continuous table acquisition MRI for radiotherapy treatment planning: distortion assessment with a new extended 3D volumetric phantom Med. Phys 42 1982–9125832089

Wang D, Strugnell W, Cowin G, Doddrell DM and Slaughter R 2004 Geometric distortion in clinical MRI systems Part I: evaluation using a 3D phantom Magn. Reson. Imaging 22 1211–2115607092

Weygand J, Fuller CD, Ibbott GS, Mohamed AS, Ding Y, Yang J, Hwang KP and Wang J 2016 Spatial precision in magnetic resonance imaging-guided radiation therapy: the role of geometric distortion Int. J. Radiat. Oncol. Biol. Phys 95 1304–1627354136

Yang Y 2016 Longitudinal diffusion MRI for treatment response assessment: preliminary experience using an MRI-guided tri-cobalt 60 radiotherapy system Med. Phys 43 1369–7326936721

Author Manuscript Author Manuscript Author Manuscript Author Manuscript

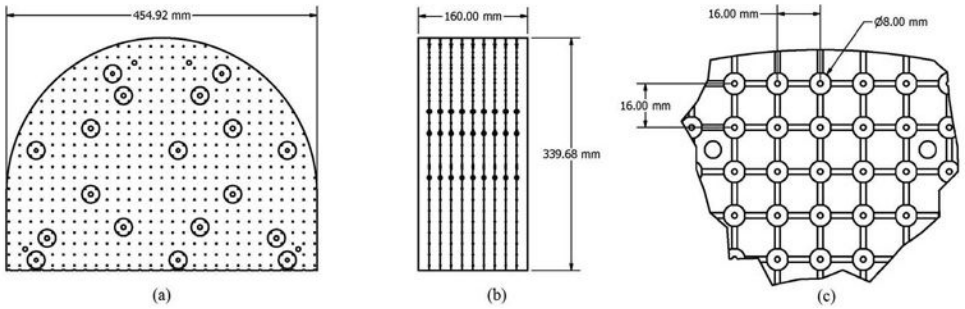

Figure 1.

A diagram of the 3D spatial integrity phantom produced by Integrated Medical Technologies: (a) the spheres (dots) and connecting rods passing through the phantom, (b) the acrylic plates stacked together forming the matrix of spheres, and (c) a small subsection of the sphere markers.

Author Manuscript Author Manuscript Author Manuscript Author Manuscript

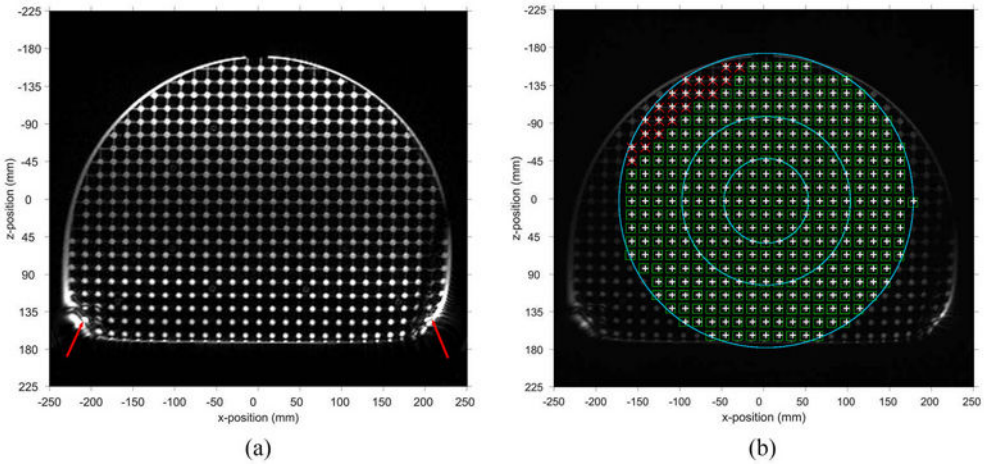

Figure 2.

The center slice of the 3D phantom showing (a) only the raw image and (b) the result of the 2D deviation analysis with the gantry at 0°, using the 1.5 mm reconstructed slice thickness scan with blue circles showing the different analysis regions. Omitted spheres in the regions with artifacts, indicated by arrows in (a), are not included in the analysis as shown along the periphery of the phantom. Only sphere locations determined within the analysis regions are shown. Ground-truth locations are represented as white '+' symbols, found sphere locations are shown as green squares if their 2D deviation is less than a 1 mm tolerance or as a red 'x' symbols if they fail.

Author Manuscript Author Manuscript Author Manuscript Author Manuscript

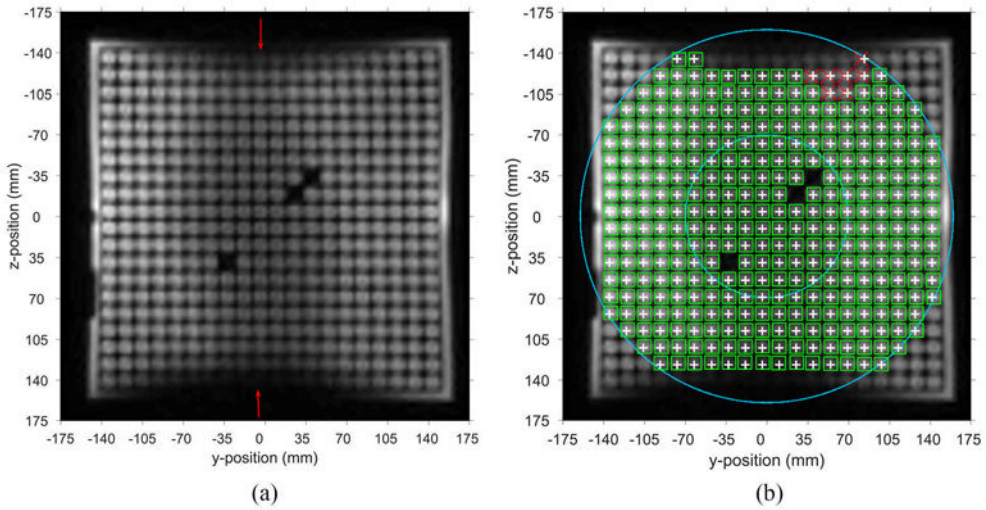

Figure 3.

Averaged image of the 2D planar phantom shifted 72 mm from isocenter. (a) The raw image, cylinders within regions of 'blurred' signal or signal losses are marked by the red arrows and were omitted from the analysis. Two of the three analysis regions are shown by the blue circles. (b) The found cylinder positions are shown as green squares if they pass the specified deviation tolerance in that analysis region, and red '*x*' markers if they fail. The tolerances used in this evaluation were 1 mm and 2 mm for the inner and outer regions respectively, the known locations are shown as white '+' symbols.

Author Manuscript Author Manuscript Author Manuscript Author Manuscript

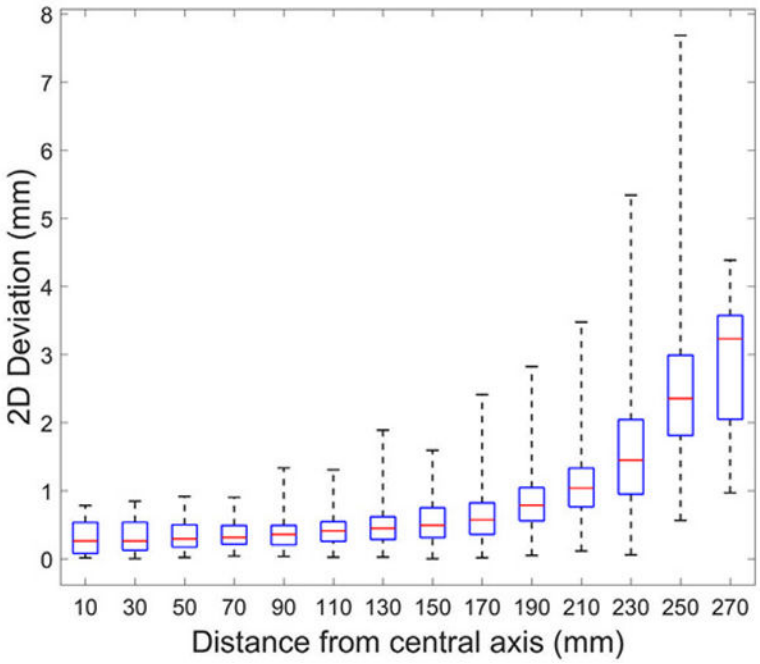

Figure 4.

The 2D deviation in the axial plane between the ground-truth and sphere locations found by the analysis software using the 1.5 mm reconstructed slice thickness scan with the gantry at 0°. The data are grouped into 20 mm bins as a function of their distance from the central longitudinal axis. The red line demarks the median deviation in each bin, the edges of the box mark the bounds of the 25th and 75th percentiles and the whiskers show the maximum and minimum data for each bin.

Author Manuscript Author Manuscript Author Manuscript Author Manuscript

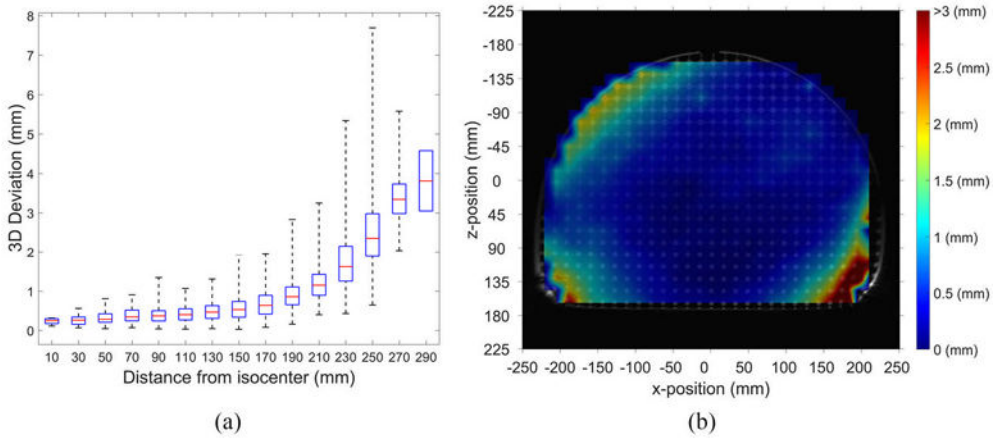

(a) (b)

Figure 5.

(a) The 3D deviation between the ground-truth and sphere locations found by the analysis software using the 1.5 mm reconstructed slice thickness scan with the gantry at 0°. The data are grouped into 20 mm bins as a function of their distance from isocenter. The red line demarks the median deviation in each bin, the edges of the box mark the bounds of the 25th and 75th percentiles and the whiskers show the maximum and minimum data for each bin. The uppermost bin contains only two data points. (b) The 3D deformation field map of the centermost axial slice of the 3D spatial integrity phantom. Imaging was conducted using the 1.5 mm reconstruction slice thickness protocol with the gantry positioned at 0°.

Author Manuscript Author Manuscript Author Manuscript Author Manuscript

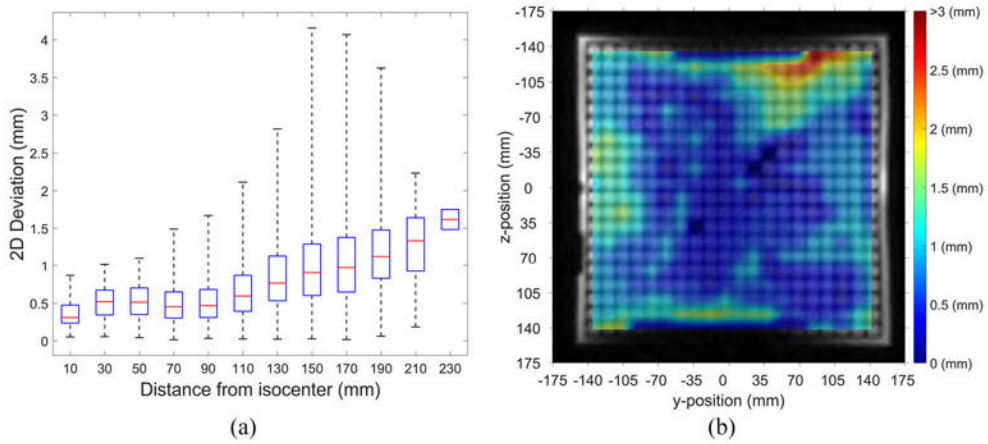

Figure 6.

(a) The 2D deviation of cylinders from their expected location with respect to their distance from isocenter using the 5 mm slice thickness real time imaging protocol and 2D spatial integrity phantom acquired across all lateral shift locations. The whiskers show the maximum and minimum data for each bin, the red line indicates the median deviation in each bin, and the edges of the box mark the bounds of the 25th and 75th percentiles of the cylinders. The final bin contains two data points, thus the boundaries of this bin correspond to these values. (b) The 2D deformation field map for the 2D spatial integrity phantom shifted 72 mm from isocenter, using the average of 40 images acquired with the 5 mm slice thickness real time imaging protocol.

Author Manuscript Author Manuscript Author Manuscript Author Manuscript

Table 1.

The acquisition parameters and simulated readout gradient amplitude for two 3D clinical bSSFP protocols commonly used at our institution for MR-guided radiotherapy.

Reconstruction slice thickness(mm)	Resolution (mm)	In-plane field of view (mm)	Slice field of view (mm)	Echo time (ms	Repetition time (ms)	Bandwidth (Hz/Px)	Flip angle (°)	Averages	Readout gradient amplitude (mT m^{-1})
1.5	1.5 × 1.5	500 × 450	432	1.45	3.37	535	60	1	8.39
3.0	1.5 × 1.5	500 × 450	432	1.27	3.00	599	60	1	9.40

Phys Med Biol. Author manuscript; available in PMC 2018 July 26.

Author Manuscript Author Manuscript Author Manuscript Author Manuscript

Table 2.

The acquisition parameters and simulated readout gradient amplitude for three 2D clinical real time bSSFP protocols commonly used at our institution for MR-guided radiotherapy.

Slice thickness (mm)	Resolution (mm)	Field of view (mm)	Echo time (ms)	Repetition time (ms)	Bandwidth (Hz/Px)	Flip angle (°)	Averages	Readout gradient amplitude (mT m^{-1})
5.0	3.5 × 3.5	350 × 350	1.09	2.49	1000	60	2	6.71
7.0	3.5 × 3.5	350 × 350	0.91	2.10	1351	60	2	9.07
10.0	3.5 × 3.5	350 × 350	0.86	2.01	1515	60	2	10.17

Phys Med Biol. Author manuscript; available in PMC 2018 July 26.

Author Manuscript

Author Manuscript

Author Manuscript

Author Manuscript

Table 3.

The average and maximum deviation in two and three dimensions for the spheres within a 50 mm, 100 mm and 175 mm radius of isocenter and entire volume for two 3D clinical scanning protocols. The passing rates for the spheres with less than 1 mm deviation within 50 mm of the center of the phantom, less than 1 mm deviation within a 100 mm radius of isocenter, less than 1 mm and 2 mm deviation within 175 mm of isocenter, and less than 2 mm deviation for all spheres in the phantom.

Reconstruction slice thickness (mm)	ROI radius (mm)	Percent passing deviation threshold			Average deviation		Maximum deviation	
		Tolerance (mm)	2D (%)	3D (%)	2D (mm)	3D (mm)	2D (mm)	3D (mm)
1.5	50	1	100	100	0.24	0.28	0.73	0.76
	100	1	99.9	99.9	0.33	0.37	1.14	1.15
	175	1	95.6	94.8	0.45	0.49	1.85	1.88
	175	2	100	100	0.45	0.49	1.85	1.88
	All	2	96.9	96.1	0.64	0.72	7.33	7.35
3.0	50	1	100	99.8	0.31	0.37	0.84	0.89
	100	1	99.5	99.1	0.39	0.43	1.17	1.22
	175	1	94.3	92.7	0.50	0.55	1.97	1.98
	175	2	96.5	95.6	0.50	0.55	1.97	1.98
	All	2	96.5	95.6	0.69	0.79	8.12	8.13

Author Manuscript

Author Manuscript

Author Manuscript

Author Manuscript

Table 4.

The average and maximum deviation in the three analysis regions and the entire volume along with the percent of cylinders with a deviation smaller than the specified tolerance using the real time imaging protocol and 2D spatial integrity phantom.

		Percent passing deviation threshold		Average deviation	Maximum deviation
Slice thickness (mm)	**ROI radius (mm)**	**Tolerance (mm)**	**2D (%)**	**2D (mm)**	**2D (mm)**
5.0	50	1	98.1	0.52	1.10
	100	1	95.0	0.51	1.67
	175	1	74.2	0.79	4.15
	175	2	96.8	0.79	4.15
	All	2	96.3	0.83	4.15